

# Onset of decoherence: Six-wave mixing measurements of vibrational decoherence on the excited electronic state of $I_2$ in solid argon

Z. Bihary, M. Karavitis, and V. Ara Apkarian<sup>a)</sup>

*Department of Chemistry, University of California, Irvine, California 92697*

(Received 20 October 2003; accepted 10 February 2004)

Pump-probe, four-wave, and six-wave mixing measurements of  $I_2$  isolated in solid argon are used to provide a clear experimental measure for the onset of vibrational quantum decoherence on the excited electronic state. The electronically resonant, six-wave mixing measurements bypass the rapid electronic dephasing, and measure the quantum cross-correlation between two packets launched on the  $B$ -state. The vibrational quantum coherence survives 1 period of motion, 400 fs, during which  $\sim 2000\text{ cm}^{-1}$  of energy is transferred to the lattice. The decoherence occurs during the second cycle of motion, while classically coherent motion measured via pump-probe spectroscopy using the same electronic resonances continues for  $\sim 15$  periods. This is contrasted with vibrational dephasing on the ground electronic surface, which lasts for  $10^2$  periods, as measured through time-resolved coherent anti-Stokes Raman scattering. The measurements and observables are discussed through time-circuit diagrams, and a mechanistic description of decoherence is derived through semiclassical analysis and simulations that reproduce the experiments. © 2004 American Institute of Physics. [DOI: 10.1063/1.1691407]

## I. INTRODUCTION

Parametric, coherent, multiwave spectroscopy with short pulses allows detailed preparation and interrogation of quantum coherences.<sup>1,2</sup> We use this tool to scrutinize the mechanics of decoherence,<sup>3</sup> namely, the breakdown of time reversal invariance of quantum evolution, which is an inescapable eventuality in real systems.<sup>4</sup> This fundamental concept, which is used to harmonize quantum and classical realities, is subject to differing definitions,<sup>5</sup> and has principally been developed in theory.<sup>6</sup> Its understanding is key to quantum control, from chemistry<sup>7</sup> to information technology.<sup>8</sup> Our intention is to use carefully crafted experiments to follow vibrational quantum coherence and its collapse with concomitant emergence of classicality. Matrix isolated molecular iodine serves as our prototype for these investigations. Pump-probe measurements serve to characterize the classical vibrational dynamics of the molecule on its excited  $B$ -state; parametric<sup>9</sup> four-wave mixing (FWM) measurements are used to characterize electronic dephasing and vibrational quantum coherence on the ground electronic  $X$ -state; and parametric six-wave mixing (SWM) measurements are used to characterize vibrational quantum coherence on the excited  $B$ -state. A succinct, yet powerful connection between observables and underlying dynamics for each of these measurements can be made through time circuit diagrams, which we will use extensively in our interpretations and analysis. The diagrams are also indispensable for the explicit simulations of the requisite quantum many-body dynamics through semiclassical initial value representation (SC-IVR).<sup>10</sup> This approach has been previously implemented to analyze absorption-emission,<sup>11,12</sup> resonant Raman,<sup>13,14</sup> and hot luminescence,<sup>15</sup> in this system.

Previously, we have reported on FWM experiments of time-resolved coherent anti-Stokes Raman scattering (TR-CARS) on iodine isolated in Ar matrices.<sup>16,17</sup> The electronically resonant TRCARS measurements establish that the  $|X\rangle\langle B|$  electronic coherence decays in less than a period of vibration, while the ground-state vibrational coherence,  $|X, v=0\rangle\langle X, v'=1,12|$ , persists for hundreds of periods. This gross information was also available in frequency domain spectra. The absence of structure on the  $B \leftarrow X$  absorption implies electronic dephasing faster than the period of vibration on the  $B$  state ( $\sim 300$  fs); and long-lived vibrational coherences on the  $X$ -state could be inferred from the line-spectrum of overtones observed in resonant Raman (RR) scattering.<sup>18</sup> A detailed semiclassical analysis of both of these processes has already been given.<sup>11</sup> Since vibrational coherences on the ground electronic state are prepared by Raman pumping of a chromophore accommodated by the lattice, dephasing occurs on a time scale long in comparison to phonon scattering times. Dephasing rates longer than the bath memory defines the weak coupling limit, where dephasing marks the destruction of all coherence. In this limit, statistical treatments of lineshapes, such as spin-Boson models,<sup>19</sup> are adequate to describe observed spectra, be it in time or frequency domain.

In contrast, when promoted to the excited electronic state, the molecule is set on a collision course with the lattice. The strongly dissipative dynamics that follows proceeds through a sequence of sharply defined “events” that are observed as wavepacket motion in time-resolved pump-probe measurements, which are faithfully reproduced through classical trajectories that do not carry any phase information.<sup>20,21</sup> Evidently, the measurements report on the evolving diagonal density, which is now better described in coordinate representation  $|B, q(t)\rangle\langle B, q(t)|$ . The deeply modulated signal es-

<sup>a)</sup>Electronic mail: aapkaria@uci.edu

establishes that in the excited electronic state, vibrational relaxation of the molecule proceeds with retention of classical correlation (population coherence). Is the quantum coherence (amplitude coherence) retained during this process? When exactly does the quantum coherence collapse during this dynamics? To answer these questions a quantum measurement of the evolving nuclear dynamics is required.<sup>22</sup> To accomplish this, we prepare a superposition of two, energetically distinct, vibrational wavepackets on the electronically excited  $B$ -state

$$\varphi(t=0) = (|\varphi_B(q_0)\rangle + |\varphi_B(q'_0)\rangle)|\psi(Q_0)\rangle, \quad (1a)$$

in which  $Q_0$  represent the bath coordinates, and the initial bath state is the thermally occupied density of the weakly coupled normal modes of the lattice with the chromophore on the  $X$ -state. The strong coupling between system and bath on the electronically excited state implies that as they evolve, each packet will drive its own distinct history in the bath

$$\varphi(t) = U(t, t_0) \varphi(t=0) = |\varphi_B(q, Q; t)\rangle + |\varphi_B(q', Q'; t)\rangle. \quad (1b)$$

The vibrational quantum coherence is then described as the deterministic evolution of the off-diagonal density

$$\rho_{BB'}(t) = |\varphi_B(q, Q; t)\rangle\langle\varphi_B(q', Q'; t)|. \quad (1c)$$

To the extent that *many*, nearly orthogonal modes of the bath are activated, (1c) describes the quantum interference term between macroscopically distinct states.<sup>6</sup> We measure the decoherence, namely the decay of (1c), through an electronically resonant parametric six-wave mixing (SWM) process; and we dissect the kinematics of decoherence through semiclassical analysis. Although not assumed in the analysis, for the sake of mechanistic insights, the anzats of orthogonal decomposition between system and bath states may be invoked

$$\rho_{BB'}(t) \approx (|q_\tau\rangle\langle q'_t|)_{\text{sys}}(|Q_t\rangle\langle Q'_t|)_{\text{bath}} = \rho_{qq'}(t) \rho_{QQ'}(t). \quad (1d)$$

This can be motivated by noting that by definition the system and bath modes are nearly orthogonal, and will decouple in time even if initially they interact strongly. Alternatively, the decomposition may be affected along the measurement states. Since the electronic resonances used are local to the chromophore coordinate, all of our projective measurements can be described after a Schmidt decomposition of the macro-system between system and bath.<sup>23,24</sup> Our purpose in invoking (1d) is to point out that decoherence can arise from the decay of either system coherence,  $\rho_{qq'}(t)$  or bath coherence,  $\rho_{QQ'}(t)$ . Although in (1d) the system and bath appear decoupled, the initial coupled evolution (1b) ensures that

they are entangled.<sup>25,26</sup> Information regarding the bath is transmitted to the system through the quantum phase, through the action  $S(t) = \int \mathcal{L}(q, Q, \dot{q}, \dot{Q}) dt$  given by the Lagrangian  $\mathcal{L}$  of the macro-system. Strong dissipation of the system, i.e., energy transfer from system to bath, is essential for establishing entanglement, and does not in itself imply decoherence. It takes time for the information transferred to the bath to degrade by generating quantum entropy, or equivalently, it takes time for the driven bath to dephase. This is the process that controls the measured vibrational decoherence on the electronically excited  $B$ -state, as we show. Since the cross-correlation between two distinct vibrational wavepackets is measured, to make such a definite assignment, it is essential to ascertain that the decay is not due to system–system overlap in the particular projective measurement. Experimentally, this is established through separate pump–probe measurements carried out individually on the same packets, using the same electronic resonances. We establish that the vibrational quantum coherence  $\rho_{qq'}(t)$  decays, while the classical cross-correlation  $[\rho_{qq}(t)\rho_{q'q'}(t)]^{1/2}$  of the system is maintained. The semiclassical simulations, which quantitatively reproduce the observations in this strong-coupling limit, allow a clear and explicit mechanistic interpretation of the measurements and the processes underlying the observations. For an insightful discussion of the semiclassical theory of coherence and decoherence in the same spirit as our development, we refer to the paper by Fiete and Heller which appeared during the review period of the present manuscript.<sup>27</sup>

The value of SWM spectroscopies in condensed media has been annunciated by Tanimura and Mukamel.<sup>28</sup> They have been pursued experimentally, because of their rich information content, and because with proper choices inhomogeneous contributions can be eliminated.<sup>29–32</sup> Here, our interest is more limited. We simply use SWM to follow the excited state vibrational coherence on time scales beyond electronic dephasing and without interference from FWM on the ground electronic state, as we describe below.

## II. THE MEASUREMENTS AND OBSERVABLES

In TRCARS the third-order material polarization,  $P^{(3)} \times(t)$ , is interrogated by monitoring the coherent anti-Stokes radiation induced with a time ordered set of three short laser pulses.<sup>33–35</sup> When limited to only two electronic states, the  $X$ - and  $B$ -states, the all-resonant FWM process is dominated by the  $P^{(0,3)}$  contribution, where the superscript (0,3) notation specified that three input pulses act on the state ket (or bra) and none act on the state bra (or ket)

$$\begin{aligned} P_{k_p - k_s + k_p'}^{(0,3)}(t_4) &= \frac{k}{\hbar^3} \int_{-\infty}^t dt_3 \int_{-\infty}^{t_3} dt_2 \int_{-\infty}^{t_2} dt_1 e^{-i(\omega_{p'} - \omega_s + \omega_p)t} \\ &\times \langle \varphi_X e^{iH_X(t_4 - t_1)/\hbar} | \hat{\mu} | e^{-iH_B(t_4 - t_3)/\hbar} \hat{\mu} E_{p'}(\mathbf{k}_{p'}, t_3) e^{-iH_X(t_3 - t_2)/\hbar} \hat{\mu} E_s^* \\ &\times (-\mathbf{k}_s, t_2) e^{-iH_B(t_2 - t_1)/\hbar} \hat{\mu} E_p(\mathbf{k}_p, t_1) \varphi_X \rangle. \end{aligned} \quad (2)$$

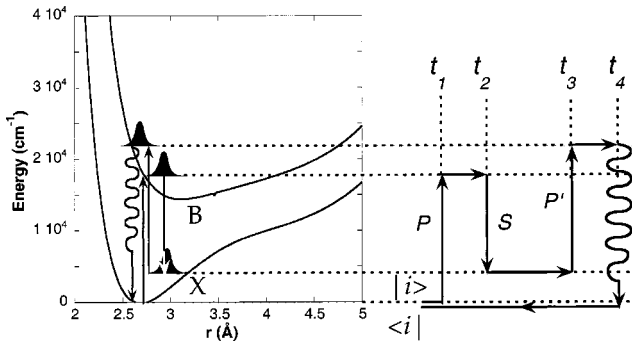


FIG. 1. Wavepacket picture and time-circuit diagram for the  $P^{(0,3)}$  contribution to third-order polarization in time-resolved coherent anti-Stokes scattering (four-wave mixing). The potentials are for molecular iodine in solid Ar, in which the attractive branch is controlled by the cage.

The process is illustrated through the time-circuit diagram of Fig. 1, which combines the content of level diagrams, double-sided Feynman diagrams, and Liouville paths.<sup>36</sup> The state bra  $\langle \varphi_X^{(0)}(t) |$  evolves field free for the duration,  $t_{41}$ . The pump (P) pulse promotes the ket to the B-state at  $t_1$ , where it evolves during  $t_{21}$  as an electronic coherence,  $|\varphi_B^{(1)}(\mathbf{k}_P, t)\rangle \langle \varphi_X^{(0)}(t) |$ , distinguished by bra and ket being on two different electronic states. At  $t_2$ , the Stokes (S) pulse dumps the ket back to X, to prepare the Raman packet  $|\varphi_X^{(2)}(\mathbf{k}_P - \mathbf{k}_S, t)\rangle$ . During  $t_{32}$ , the system is in a vibrational coherence on X. At  $t_3$ , the probe ( $P'$ ) pulse promotes the Raman packet back to B, where it evolves until it radiates at  $t_4$ . Radiation closes the time circuit by projecting the ket on the bra. The measured signal is the time integrated anti-Stokes polarization,  $\int dt_4 |P^{(3)}(t_4)|^2$  propagating along  $\mathbf{k}_{AS} = \mathbf{k}_P - \mathbf{k}_S + \mathbf{k}_{P'}$  (throughout we will be concerned with three noncollinear input beams in two different colors,  $\omega_S < \omega_P = \omega_{P'}$ ). The measurement, as expressed by (2), selects a particular Fourier component of the quantum three-time correlation (the argument of the Fourier integral), which may be transcribed in terms of density matrices

$$C(t_{43}, t_{32}, t_{21}) = \text{Tr}[\hat{\mu} \hat{U}(t_{43}) \hat{V}(\mathbf{k}_{P'}, t_3) \hat{U}(t_{32}) \hat{V}^+ \times (-\mathbf{k}_S, t_2) \hat{U}(t_{21}) \hat{V}(\mathbf{k}_P, t_1) \rho_{XX} \hat{U}^+(t_{41})], \quad (3a)$$

in which  $\rho_{XX} = |X\rangle e^{-\beta H} \langle X|$  is the thermal density on the ground electronic state, and the time evolution and interaction operators,  $\hat{U}$  and  $\hat{V}$ , should be clear from (2). Recognizing the time-reversal identity,  $\hat{U}(t_{14}) = \hat{U}^+(t_{41})$ , all operators can be made to act from the left

$$C(t_{43}, t_{32}, t_{21}) = \text{Tr}[\hat{U}(t_{14}) \hat{\mu} \hat{U}(t_{43}) \hat{V}(\mathbf{k}_{P'}, t_3) \hat{U}(t_{32}) \hat{V}^+ \times (-\mathbf{k}_S, t_2) \hat{U}(t_{21}) \hat{V}(\mathbf{k}_P, t_1) \rho_{XX}]. \quad (3b)$$

Now the evolution is restricted to the state ket. The ket is projected with the various fields as it evolves forward in time, then after radiation,  $\hat{\mu} = |X\rangle \mu \langle B|$ , it evolves backward in time to close the loop (see the sense of arrows in Fig. 1). The forward-backward interpretation of the time-circuit diagram transmits the mechanistic insight, that: *The coherence measures the reversibility of the quantum dynamics around*

*the circuit.* This is the central concept in our analysis, and at the core of semiclassical forward-backward initial value representation in evaluating quantum observables of complex systems.<sup>37,38</sup> For Hamiltonian evolution over eigenstates, the reversibility requirement simply establishes the resonances in the four-wave interaction between fields and matter—multiples of  $2\pi$  phase must be accumulated around the circuit.<sup>39</sup> In dissipative systems, or strongly coupled systems with large densities of states, it is the periodicity of action that is interrogated through the reversibility criterion. Randomization of the action angle with time, as the circuit stretches in time, signifies decoherence.

While any measurement involves the entire circuit, pulse sequences can be chosen to dissect decoherence over a particular segment. This is accomplished by separating evolution, from preparation and interrogation. For example, to interrogate the electronic coherence,  $\rho_{BX}(t_{21})$ :

$$\begin{aligned} \rho_{BX}(t_{21}) &= |\varphi_B^{(1)}(\mathbf{k}_P, t)\rangle \langle \varphi_X^{(0)}(t)| \\ &= \hat{U}(t_{21}) \hat{V}(\mathbf{k}_P, t_1) \rho_{XX} \hat{U}^+(t_{21}), \end{aligned} \quad (4)$$

the signal is collected as a function of  $t = t_{21}$  with fixed  $P'$ - and S-pulses. What is measured is the correlation

$$\begin{aligned} c_{BX}(t_{21}) &= \text{Tr}[\hat{W}(\Delta t) \rho_{BX}(t)] \\ &= \langle \varphi_X^{(0)}(t) | \hat{W}(\Delta t) | \varphi_B^{(1)}(\mathbf{k}_P, t) \rangle, \end{aligned} \quad (5)$$

in which the  $P'/S$  pulses serve as an indirect projection between the packets on the X- and B-surfaces through the window which operates as

$$\hat{W}(\Delta t) = \hat{U}^+(t_{42}) \hat{\mu} \hat{U}(t_{43}) \hat{V}(\mathbf{k}_{P'}, t_3) \hat{U}(t_{32}) \hat{V}^+(-\mathbf{k}_S, t_2). \quad (6)$$

To reproduce the magnitude of the measurable polarization and its profile, it is essential to include evolution under the window during  $\Delta t = t_{42}$ . However, to the extent that the coherence is not destroyed under the probe window (hence the preferred choice  $t_{32} \rightarrow 0$ ), the signal as a function of  $t_{21}$  yields the time evolution of the electronic coherence  $\rho_{BX}$ . The same coherence is also involved over the  $t_{43}$  interval. Information about this period of evolution is contained in the time-frequency profile of the anti-Stokes radiation, which can be analyzed through gated detection.<sup>40</sup>

The vibrational coherence on the ground electronic state,  $\rho_{X'X}(t_{32})$ , is interrogated by scanning  $t = t_{32}$ , with a fixed delay between P and S-pulses. Even if coincident P/S pulses are chosen ( $t_{21} \rightarrow 0$ ), since the Raman packet is prepared through a real electronic resonance, it will necessarily contain the history of evolution on the excited B-surface

$$\begin{aligned} \rho_{X'X}(t_3) &= |\varphi_X^{(2)}(\mathbf{k}_P - \mathbf{k}_S, t)\rangle \langle \varphi_X^{(0)}(t)| \\ &= \hat{U}(t_{32}) \hat{V}^+(-\mathbf{k}_S, t_2) \hat{U}(t_{21}) \hat{V}(\mathbf{k}_P, t_1) \\ &\quad \times \rho_{XX} \hat{U}^+(t_{21}) \hat{U}^+(t_{32}). \end{aligned} \quad (7)$$

Now, the signal is the projective measurement of the correlation between the stimulated Raman packet and the initial state

$$c_{X'X}(t) = \text{Tr}[\hat{W}(\Delta t) \rho_{X'X}(t_{32})] \\ = \langle \varphi_X^{(0)} | \hat{W}(\Delta t) | \varphi_X^{(2)}(\mathbf{k}_P - \mathbf{k}_S, t_{32}) \rangle, \quad (8)$$

with the window operator defined as

$$\hat{W}(\Delta t, t_3) = \hat{U}^+(t_{43}) \hat{\mu} \hat{U}(t_{43}) \hat{V}(\mathbf{k}_{P'}, t_3). \quad (9)$$

The decay of the signal can be associated with the vibrational decoherence to the extent that the histories under  $t_{21}$  and  $t_{43}$  are negligible. In practice, evolution on the excited electronic state during  $t_{21}$  is crucial to prepare high lying vibrations in the Raman packet. During this period, solvent coordinates coupled to the chromophore experience a momentum kick—the measurement perturbs the bath. Also, fast electronic dephasing during  $t_{43}$  dictates that only the negative momentum component of the vibrational coherence can be observed, since the positive momentum component when vertically projected is doomed by electronic dephasing prior to returning to the Franck–Condon window—the projector (9) also acts as a momentum filter.<sup>16</sup> To be sure, the observable vibrational coherence is effected by the measurement, both through preparation and detection steps.

Now consider the  $P^{(1,2)}$  contribution to TRCARS, in which bra and ket are both promoted to the  $B$  state, and the

$$P_{\text{AS}}^{(1,2)}(t) = \frac{c}{\hbar^3} \int_{-\infty}^t dt_3 \int_{-\infty}^{t_3} dt_2 \int_{-\infty}^{t_2} dt_1 e^{-i(\omega_{P'} - \omega_S + \omega_P)t} \times \langle \varphi_X e^{iH_X(t_2 - t_1)/\hbar} \hat{\mu} E_S^* \\ \times (-\mathbf{k}_S, t_2) e^{iH_B(t_4 - t_2)/\hbar} | \hat{\mu} | e^{-iH_*(t_4 - t_3)/\hbar} \hat{\mu} E_{P'}(\mathbf{k}_{P'}, t_3) e^{-iH_B(t_3 - t_1)/\hbar} \hat{\mu} E_P(\mathbf{k}_P, t_1) \varphi_X \rangle. \quad (10)$$

Note, since the bra is promoted to the  $B$  state with the complex  $S$ -field,  $E_S^*$ , a down-arrow is used to describe this action in the time-circuit diagram. The contribution of (10) to TRCARS has been identified in iodine vapor.<sup>39,41</sup> If we contract  $t_{21}$  by choosing coincident  $P/S$ -pulses,  $P^{(1,2)}(t_{32})$  measures the vibrational coherence on the  $B$ -state

$$\rho_{B'B}(t_{32}) = |\varphi_B^{(1)}(\mathbf{k}_P, t) \rangle \langle \varphi_B^{(1)}(-\mathbf{k}_S, t) | \\ = \hat{U}(t_{32}) \hat{V}(\mathbf{k}_P, t_2) \rho_{XX} \hat{V}^+(-\mathbf{k}_S, t_2) \hat{U}^+(t_{32}). \quad (11)$$

This is the target of our investigation. However, the disadvantage of this FWM scheme is that it has the same time sequence of input pulses, and the same AS spectrum and propagation vector as the  $P^{(0,3)}$  contribution from the vibrational coherence on the ground-state (7). The latter masks the excited state signal, as we will show. The SWM experiments, which we discuss below, overcome this difficulty. Let us first contrast the excited state vibrational coherence measured in FWM with that observed in pump–probe measurements.

Pump–probe is also a four-wave process, however in contrast with the parametric TRCARS process,<sup>9</sup> the signal reports on both the diagonal and off-diagonal vibrational density on the excited state. Pump–probe measurements with

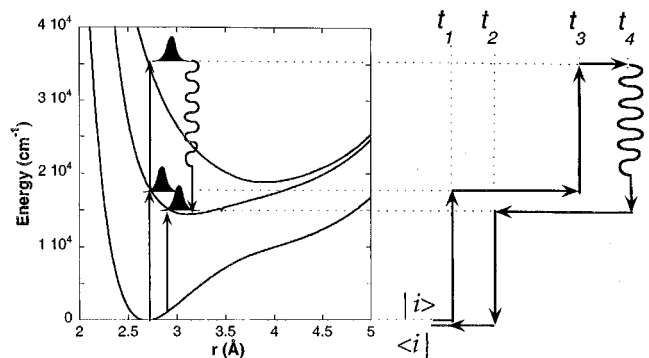


FIG. 2. Wavepacket picture and time-circuit diagram for the  $P^{(1,2)}$  contribution to third-order polarization in time-resolved coherent anti-Stokes scattering (four-wave mixing). To be electronically resonant, in addition to the  $X$ - and  $B$ -states, a third electronic state must be involved.

correlation between these first order packets is interrogated with the  $P'$ -pulse, see Fig. 2. To be comparable in intensity with the  $P^{(0,3)}$  signal, the process must be electronically resonant in all interactions, hence the inclusion of a third electronic state in Fig. 2. Identifying the vibrational Hamiltonian of the third electronic state as  $H_*$  the time-circuit of Fig. 2 transcribes to

two pulses that are not phase-locked, correspond to two successive excitations in which the observable, such as fluorescence (see Fig. 3), is the product of two different transition probabilities. Each excitation process measures a single time correlation, evident when considering the absorption probability due to the pump pulse

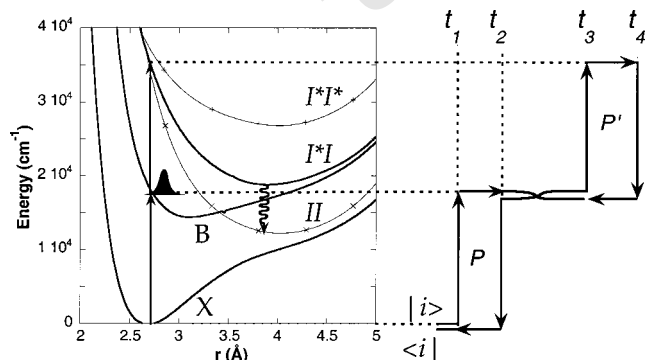


FIG. 3. Wavepacket picture and time-circuit diagram for pump-probe measurements. The crossing of the bra and ket time-lines during  $t_{32}$  signifies collapse of the vibrational coherence on the electronically excited state.



$$\begin{aligned} \sigma(\omega_P) = & \int_{-\infty}^{\infty} dt e^{-i\omega_P t} \langle \varphi_X | e^{iH_X(t_2-t_1)/\hbar} \hat{\mu} E^*(\mathbf{k}_P, t_2) \\ & \times e^{-iH_B(t_2-t_1)/\hbar} | \varphi_B \rangle \langle \varphi_B | \hat{\mu} E_P(\mathbf{k}_P, t_1) | \varphi_X \rangle, \end{aligned} \quad (12a)$$

or, equivalently

$$\sigma(\omega) = \int dt e^{-i\omega t} \rho_{XB}(t). \quad (12b)$$

$$\begin{aligned} I_{\text{pu-pr}}(t) = & \frac{c}{\hbar^3} \int_{-\infty}^{t_4} dt_3 e^{-i\omega_P t_3} \int_{-\infty}^{t_3} dt_2 \int_{-\infty}^{t_2} dt_1 e^{-i\omega_P t_1} \\ & \times \langle \varphi_X | e^{iH_X(t_2-t_1)/\hbar} \hat{\mu} E_P^*(t_2) e^{iH_B(t_4-t_2)/\hbar} \hat{\mu} E_P^*, e^{-iH_*(t_4-t_3)/\hbar} \hat{\mu} E_{P'}(t_3) e^{-iH_B(t_3-t_1)/\hbar} \hat{\mu} E_P(t_1) \varphi_X \rangle. \end{aligned} \quad (13)$$

This bears a close resemblance to the  $P^{(1,2)}$  polarization (10). The two processes interrogate different Fourier components of otherwise nearly identical three-time correlations. Diagrammatically, pump-probe consists of two loops defined by the two Fourier filters active under the two time-separated pulses, as illustrated in Fig. 3—the difference in pump-probe versus  $P^{(1,2)}$  lies in the crossing of the time histories of bra and ket during  $t_{32}$ . This becomes particularly significant in the presence of vibrational decoherence on the  $B$  state. When the off-diagonal density  $\rho_{BB'}$  decays, so does the CARS signal but not the pump-probe signal. Just as in the case of the  $P$ -pulse, which acts on the  $\rho_{XX}$  population to create a coherence by splitting bra and ket, so does the  $P'$ -pulse act on the  $B$ -state population,  $\rho_{BB}$ . The distinction between bra and ket on the  $B$ -state is lost due to the absence of a phase matching condition. To the extent that the population is created and interrogated impulsively with non overlapping pulses, we may set  $t_2 = t_1 = 0$  and  $t = t_{32}$  and identify

$$\rho_{BB}(t=0) = V(\omega_P) \rho_{XX} V^\dagger(\omega_P), \quad (14a)$$

to recognize that the pump-probe measurement yields

$$\begin{aligned} S(t) &= \text{Tr}[\rho_{BB}(t) W(\omega_{P'})] \\ &= \text{Tr}[\hat{V}(\omega_{P'}) \rho_{BB}(t) \hat{V}^\dagger(\omega_{P'})] = \rho_{BB}(t) \delta[\mathbf{q} - \mathbf{q}^*], \end{aligned} \quad (14b)$$

where  $\mathbf{q}^*$  is given by the energy conservation condition,  $\delta[\hbar\omega_{P'} - \Delta V(\mathbf{q}^*)]$  in which  $\Delta V(\mathbf{q})$  is the difference potentials involved in the probe transition. Thus, the roles of pump and probe are reduced to doorway and window of the semiclassical Franck-Condon approximation.<sup>42-45</sup> This is the basis of the validity of simulations that rely strictly on classical molecular dynamics, in which a swarm of trajectories plays the role of  $\rho_{BB}$ . In essence, pump-probe allows a classical measurement of the evolving vibrational coherence, while the FWM experiment of Fig. 2 is strictly a quantum measurement.

The absorption spectrum is the Fourier transform of the electronic coherence that consists of the single time-loop over  $t_{21}$ . According to (12a), the field projects the  $X$ -state ket on the  $B$ -state at  $t_1$ , where it evolves forward in time, until field projected back at  $t_2$ , where it evolves backward in time to close the loop. The same holds for the action of the  $P'$ -pulse, except now the transition is between the  $B$ -state and a higher lying electronic state. The intensity of the pump-probe signal with nonoverlapping pulses can be written as

Given a choice of colors to implement all-resonant FWM, increasing field intensities alone will give rise to the next order resonant parametric process, which in an isotropic medium corresponds to six-wave mixing that measures the fifth-order polarization  $P^{(5)}(t)$ . With  $P$ - and  $S$ -pulses in overlap, increasing intensities enables the SWM process of Fig. 4, among others. In this process, the ket is acted on by  $2\mathbf{k}_P - \mathbf{k}_S$ , while the bra is acted on by  $-\mathbf{k}_S$ , to launch two vibrational packets on the  $B$ -state. The  $P'$ -pulse then acts resonantly via the third electronic state to produce the 6th wave along  $2\mathbf{k}_P - 2\mathbf{k}_S + \mathbf{k}_{P'}$  at  $\omega = 3\omega_P - 2\omega_S$ . Both spatially and spectrally the SWM signal is distinct from the FWM signal. As a function of probe pulse delay,  $P^{(1,4)}(t_{32})$  measures the vibrational coherence  $|\varphi_B^{(3)}(2\mathbf{k}_P - \mathbf{k}_S; t)\rangle \langle \varphi_B^{(1)}(-\mathbf{k}_S; t)|$ . Save for the difference in the relative energy of packets, the measurement is identical to that obtained through  $P^{(1,2)}$  (compare Figs. 2 and 4); however, in contrast with the latter, the fifth-order polarization measured in SWM does not interfere with the third-order polarization measured in TRCARS.

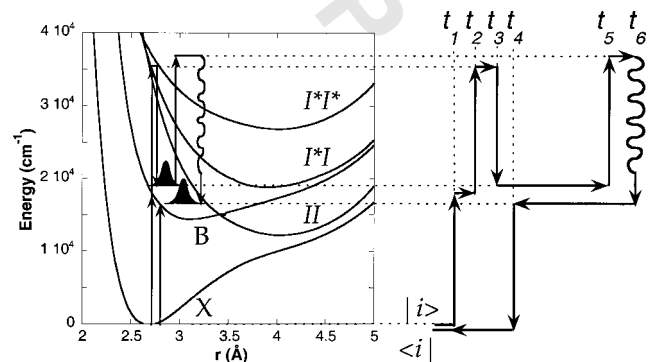


FIG. 4. Wavepacket picture and time-circuit diagram for the  $P^{(1,4)}$  contribution to fifth-order polarization in six-wave mixing. The experiments are carried out with coincident pump and Stokes pulses, therefore, the indicated time-ordering of the  $P$ - and  $S$ -actions is not unique.

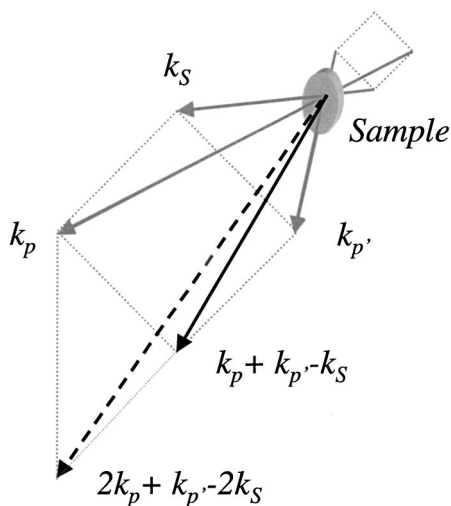


FIG. 5. The experimental arrangement in forward boxcars geometry, showing the directions for four-wave and six-wave mixing signals.

### III. EXPERIMENT

The experiments are conducted on thin films of  $I_2$ -Ar matrices, at a dilution of 1/5000, prepared by deposition of the premixed gas on a sapphire window held at 32 K. The pulsed deposition conditions are adjusted to produce samples with minimal optical scattering. The laser pulses are obtained from two optical parametric amplifiers (OPA), pumped by a regeneratively amplified, Kerr lens mode-locked Ti:Sapphire laser, which in turn is pumped with an Ar-ion laser. The measurements are conducted in the BOXCARS geometry illustrated in Fig. 5. The two pump beams,  $P$  and  $P'$ , are derived by splitting the doubled output of one OPA, the Stokes beam is obtained from the second OPA. The three noncollinear beams are focused onto the sample through a single achromat. The pulses are nearly transform limited, with a width of  $\sim 80$  fs.

The coherent polarization radiating along a direction dictated by the momentum matching condition for a given non-linear mixing process is selected by spatial filtering, using an iris diaphragm. The anti-Stokes radiation due to FWM propagates along

$$k_{AS} = k_p + k_{p'} - k_S. \quad (15)$$

The sought SWM polarization, with a delayed  $P'$  pulse, radiates along

$$k_6 = 2k_p + k_{p'} - 2k_S. \quad (16)$$

The directions are shown in Fig. 5. Spatial filtering is only partially effective in the films we prepare. Because of scattering, several beams contribute to radiation in a given solid angle. This allows the simultaneous collection of the spectrally distinguishable FWM and SWM signals. The AS radiation in the FWM mixing process occurs at

$$\omega_{AS} = 2\omega_p - \omega_S, \quad (17)$$

while the 6-wave mixing process of interest occurs at

$$\omega_6 = 3\omega_p - 2\omega_S. \quad (18)$$

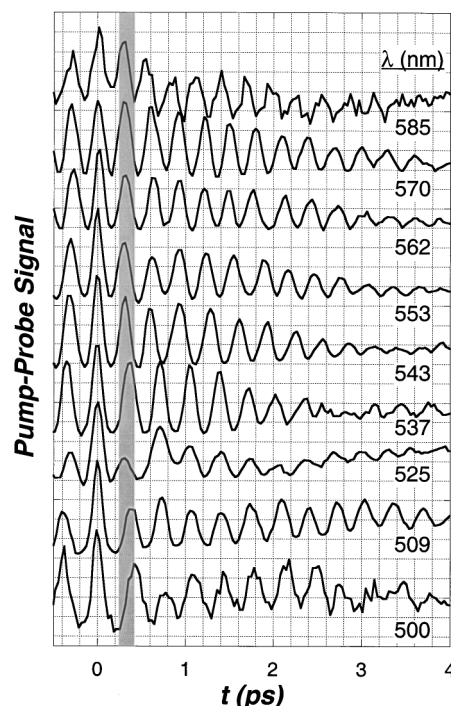


FIG. 6. Single color pump-probe measurements at indicated wavelengths. Fluorescence at 1340 nm is used as signal. The gray stripe marks the timing of the six-wave signal, and shows the coincidence of the first recursions for the different initial preparations.

The radiation picked up through an iris placed between the  $P'$  and AS propagation directions is dispersed with a 1/4-m monochromator, and the spectrum is recorded and averaged on a CCD array. The entire spectrum is recorded for a given time delay, producing a two-dimensional map on the  $\omega$ - $t$  plane. The 6-wave measurements are carried out with  $\sim 1$   $\mu$ J pulses focused down to a spot size of 35  $\mu$ m [full width at half maximum (FWHM)]. The quadrilinear FWM measurements are carried out with  $\sim 100$  nJ pulses.

The same apparatus is used to carry out single-color pump-probe measurements. Upon visible excitation of iodine to the  $B$ -state, there are several upper electronic states that can be used to probe the evolving dynamics. The data we present is obtained by monitoring the spin-flip transition at 1340 nm (fluorescence decay time of 200 ns),<sup>46</sup> using a 1/4-monochromator and liquid nitrogen cooled germanium detector.

### IV. RESULTS

Single color pump-probe data is presented in Fig. 6, for laser wavelengths ranging from 585 to 500 nm. The wavelength range is dictated by detectivity of the signal, at either extreme the S/N ratio degrades due to loss of absorption intensity. The measurements are carried out with nearly equal intensities in the pump and probe beams. As such, the signal is symmetric with respect to the time origin. The oscillatory part of the signal, which occurs over a nonzero background, is strictly due to wavepacket motion on the  $B$ -state. This is easily identified by the period of motion of  $\sim 300$  fs, which is characteristic to the  $B$ -state. The provided gridline enables comparisons of the recursions for packets

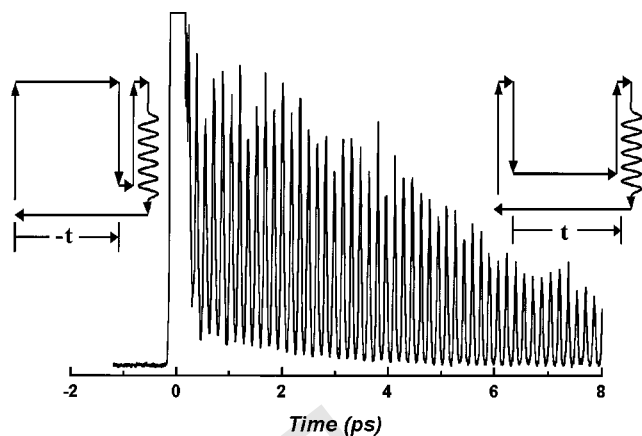


FIG. 7. The quadrilinear CARS signal obtained with  $\lambda_P=550$  nm and  $\lambda_S=595$  nm. The time sequence of pulses is illustrated in the insets. At positive time, the coherence of the vibrational superposition in the Raman packet centered at  $v=7$  of the ground electronic state is measured. At negative time the electronic coherence is probed. The absence of signal outside the overlap of pulses indicates that the electronic dephasing occurs on a time scale shorter than the period of vibration on the  $B$ -state.

launched with different initial energies. Since both pump and probe wavelengths are changed, both initial energy of the packet and the location of probe window changes in each scan. The signal decays with time due to the combination of effects: Vibrational cooling drops the packet out of the probe window, predissociation leads to leakage of the  $B$ -state population, and wavepacket spreading broadens the resonances.

The quadrilinear four-wave TRCARS signal obtained with  $\lambda_P=550$  nm and  $\lambda_S=595$  nm is shown in Fig. 7. The data is obtained with a coincident pair of P/S-pulses, while the  $P'$ -pulse is scanned in time. The pulse sequences associated with our convention for the sense of time is shown in the insets to Fig. 7. At negative time the electronic coherence between  $X$ - and  $B$ -states is probed, while at positive time the vibrational coherence on the  $X$ -state is probed. The electronic coherence is not measurable outside the overlap of all three pulses, while the vibrational coherence can be followed for  $10^2$  recursions with a period of 160 fs, characteristic to the  $X$ -state.

The strong-field signal, obtained with the same colors as in the quadrilinear FWM, is shown as a two-dimensional (2D) map in Fig. 8. Three spectral components can be seen at positive time. Light from the transmitted  $P'$ -beam can be seen at  $\lambda=550$  nm (scatter from the  $S$ -beam is rejected by a short-pass filter). The CARS signal appears at  $\lambda=500$  nm [Eq. (7)]. The SWM signal appears at  $\lambda=465$  nm [Eq. (8)], at a delay of 330 fs with a width of 170 fs. Under the assumption of direct SWM, the signal can be uniquely assigned to the process illustrated in Fig. 4. Its color, at  $3\omega_P - 2\omega_S$ , identifies it as parametric SWM. Its timing corresponds to a full period of motion on the  $B$ -state, identifying the probe resonance to be the same as that of the pump-probe measurement (Fig. 6). The signal does not carry spectral structure, implying that the radiation occurs promptly. Since the coherence is interrogated with the delayed  $P'$ -pulse, it must be prepared with  $2k_P - 2k_S$ . It remains to consider the possible distribution of these four interactions

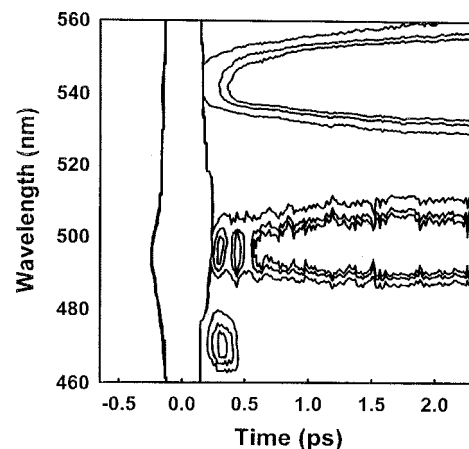


FIG. 8. Two-dimensional plot of the scattered radiation in strong-field excitation. The structureless trail at 550 nm is the leakage of the pump pulse. The structured trail at 495 nm ( $2\omega_P - \omega_S$ ) is the strong field FWM signal. The single peak at 475 nm ( $3\omega_P - 2\omega_S$ ) can be uniquely identified as the SWM signal illustrated in Fig. 4.

on bra and ket state vectors under the coincident  $P/S$  pulses. Any even number of actions on bra (or ket) is unacceptable, since this could not prepare the  $B$ -state. Three interactions must act on bra (or ket) and one must act on ket (or bra). To radiate at  $3\omega_P - 2\omega_S$ , the polarization must be prepared with  $2k_P - k_S$  acting on ket and  $-k_S$  acting on bra, with  $k_{P'}$  acting on ket as probe. The detected signal consists of the fifth order polarization,  $P^{(1,4)}$ , given by the diagram in Fig. 4. The only possible cascaded FWM processes are trivially related to the SWM. Instead of direct preparation of  $|2k_P - k_S\rangle\langle -k_S|$ , it is possible to consider the process to be sequential, mediated by the field generated at  $2k_P - k_S$  (or  $-k_S$ ) acting on the rest of the ensemble. Phase retardation between the cascaded versus direct process could effect the overall intensity of the signal. Since absolute intensities are not measured, the distinction is inconsequential in the present homodyne measurements.

Spectrally integrated time profiles of the three components seen in the contour plot are stacked in Fig. 9. The comparison contains valuable information.

The envelope of the strong-field FWM signal closely follows the time profile of the transmitted  $P'$ -beam. After the initial decay of the  $t=0$  signal, the strong-field FWM signal grows on the time scale of 2 ps. This is to be contrasted with the quadrilinear TRCARS signal shown in Fig. 7, which decays monotonically. This suggests that the envelope of the FWM signal is determined by attenuation of the  $P'$ -field due to excited-state absorptions. The 2 ps rise-time is consistent with the decay of the pump-probe signal at 550 nm, due to vibrational cooling of the  $B$ -state packet. As the  $B$ -packet falls out of the absorption window through vibrational cooling, the attenuation of the  $P'$  beam subsides, and the nonlinear processes gain intensity.

While the weak-field TRCARS signal shows a regular modulation (see Fig. 7), modulation in the strong-field FWM signal is irregular, indicating interference from several contributions. In addition to the  $X$ -state frequency of  $200\text{ cm}^{-1}$ , Fourier analysis shows significant contributions at 60 and

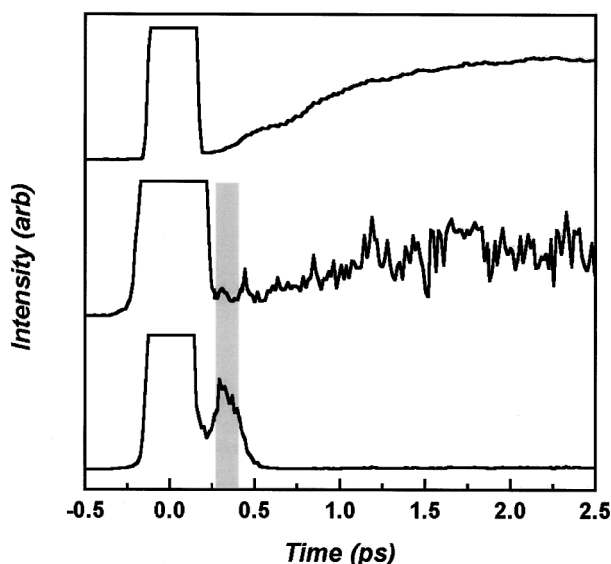


FIG. 9. The spectrally integrated time profiles of the signals shown in Fig. 8. The leakage of the structureless pump pulse (top trace) grows in time, indicating reduced absorption. The structure in the strong-field FWM signal is irregular (compare to the weak field FWM signal in Fig. 7) as a result of interference from multiple sources, including TRCARS from the stationary state population developed in  $A/A'$  state. The SWM signal (lower trace) shows a single, broad time resonance centered at a delay of 330 fs.

$112\text{ cm}^{-1}$ . These interference terms cannot be assigned to vibrational dynamics on either  $B$  or  $X$  states. They can, however, be assigned to TRCARS arising from the  $A'$  state, which has a radiative lifetime of 6 ns,<sup>47</sup> and therefore, under 1 KHz irradiation develops a steady-state population. Despite the irregularity of the FWM signal, the shaded resonance in Fig. 9 can be seen to coincide with that of the SWM signal. This is consistent with the expected  $P^{(1,2)}$  contribution in FWM, which is closely related to the SWM process (compare diagrams in Figs. 2 and 4).

## V. DISCUSSION

### A. Impulsive decoherence through electronic dephasing

Consider the TRCARS signal of Fig. 7. The absence of signal at negative time ( $-t \equiv t_{21}$ , see inset to Fig. 7) indicates that the electronic coherence decays without recursions. Evidently, the electronic dephasing time  $1/\gamma_{BX}$  is shorter than a period of motion on the  $B$ -state:  $1/\gamma_{BX} < 300\text{ fs}$ . This was already known from the lack of structure in the absorption spectrum, through the Fourier relation (12b). Information on shorter time scale regarding this process is contained in the intensity profile of the vibrational progression observed in resonant Raman spectra.<sup>13</sup> The observed profiles have been reproduced through semiclassical simulations in coordinate representation, to conclude that the electronic coherence decays on a time significantly shorter than the half-period of motion on the  $B$ -state.<sup>11</sup> The onset of decoherence is in the vibrationally impulsive regime. Along coordinates coupled to the chromophore, phase space overlap between ground and excited states starts to decay as momentum builds in the excited state. The  $n$ -body wavepackets are even-

tually displaced due to the difference between molecule–lattice interactions in the ground and excited states (electron–phonon coupling). Although the loss of correlation along any one coordinate is small, the involvement of *many* ensures that the collective coherence decays irreversibly.<sup>11</sup>

### B. Vibrational decoherence through dephasing—weak coupling limit

At positive time, the TRCARS signal in Fig. 7 interrogates the vibrational coherence on the ground electronic state through the correlation between the prepared Raman packet and the initial thermal density (8). The coherence is seen to last for hundreds of vibrations of chromophore and lattice. Clearly, we are in the limit of weak coupling, where the standard decomposition of the Hamiltonian into a sum of system, bath and interaction,  $H = H_s + H_b + H_{s-b}$ , is applicable. Substituting this in the time-evolution operators in (3), and after tracing over the bath, the system coherence is described in the vibrational basis:

$$\begin{aligned} \rho_{X'X}(t)_{\text{sys}} &= Tr_{\text{bath}}[\rho_{X'X}(t)] \\ &= \sum_v a_v e^{-i\omega_{v0}t} e^{-\gamma_{X'X}(v)t} |v\rangle\langle 0|. \end{aligned} \quad (19)$$

In which  $\omega_{v0} = (E_v - E_0)/\hbar$  and the vibration dependent decay rates,  $\gamma_{X'X}(v)$ , represent the sum of pure dephasing and dissipation. The signal can be fit by reducing the preparation and interrogation (under  $t_{21}$  and  $t_{43}$  of the circuit in Fig. 1) to a single Gaussian convolution

$$S(t) = \int dt |P^{(0,3)}(t)|^2 \propto \int d\tau G(t - \tau, \Delta t) |\rho_{X'X}(t)_{\text{sys}}|^2. \quad (20)$$

The good agreement of this treatment with experiments establishes that the evolution of the system is nearly diagonal in the molecular vibrational basis.<sup>16,17</sup> Moreover, for the prepared superposition near  $v=7$ , the perturbation of the bath during  $t_{21}$  does not have a measurable signature. The dephasing is due to the thermally occupied phonons, as diagnosed through the temperature dependence of  $\gamma(v)$ .<sup>17</sup> It is possible to argue that the coupling to the environment selects the molecular vibrations as the proper system states. In the literature on decoherence, this process is referred to as “einselection,” and the system states that minimize decoherence are identified as the “einstates.”<sup>48</sup> The coherence decays in this case through phase damping among the vibrational states, due to the noise accumulated through the link to the thermal bath. Vibrational decoherence on the ground electronic state is rate limited by dephasing of the system.

### C. Classically coherent vibrational dissipation

The pump–probe data of Fig. 6 define the essential system parameters for the interpretation of the excited state vibrational dynamics. At all wavelengths, the signal shows a peak at  $t=0$ . This locates the probe window to be vertically above the pump window—the vibrational packet is probed from the inner turning point of the  $B$ -state. Since the monitored fluorescence at  $\lambda = 1340\text{ nm}$  has been previously assigned to the spin–flip transition  $I^*I^* \rightarrow I^*I$ ,<sup>46</sup> the probe tran-



sition may be assigned to  $I^*I^*(^1\Sigma_{0g^+}) \leftarrow B(^3\Pi_{0u^+})$ . The gridlines provided in Fig. 6 enable comparisons of recursion times for different excitations. Between 585 and 543 nm, the first recursion occurs near 300 fs, the motion is nearly harmonic, with 13 recursions completed in 4 ps. In this region, the solvated  $B$ -potential may be assigned a harmonic frequency of  $\omega_e = 110 \text{ cm}^{-1}$ . At shorter wavelengths, the first period elongates, reaching  $t = 420 \text{ fs}$  at 500 nm. Also, the recursion amplitude becomes irregular due to feedback from the driven cage. This is most prominently observed at 525 nm, in which the first recursion peak is smaller than the second. In time, the recursion periods reach the harmonic limit of 300 fs. At these excitation energies, the system undergoes rapid and nonlinear vibrational relaxation. This process has been analyzed in some detail in solid Kr, and experiments are found to be in excellent agreement with the classical simulations.<sup>20,49</sup> To establish quantitative system parameters, we carry out similar simulations for the present case of  $I_2$ -Ar.

The principles and procedures for reconstructing pump-probe signals through classical simulations are well established. In the present, we use a simulation cell containing two mobile layers of the host (72 Ar atoms) surrounded by a stationary cell fixed at the lattice equilibrium position. The I-I potential in the  $B$ -state is treated as a Morse ( $D_e = 4747 \text{ cm}^{-1}$ ,  $\beta = 1.6 \text{ \AA}^{-1}$ ,  $r_e = 3.108 \text{ \AA}$ ), the Ar-Ar interactions are treated as Lennard-Jones ( $\epsilon = 80.6 \text{ cm}^{-1}$ ,  $\sigma = 3.4 \text{ \AA}$ ), and the I-Ar interactions are treated as Morse ( $D_e = 130.1 \text{ cm}^{-1}$ ,  $\beta = 1.586 \text{ \AA}^{-1}$ ,  $r_e = 4.133 \text{ \AA}$ ). The trajectories are sampled from an initial thermal distribution, at an effective temperature of 40 K. The I-I distance is then stretched to match a particular excitation energy, the potential is switched to that of the excited state, and trajectories are propagated. The signal is evaluated according to (14)

$$S(t) = \text{Tr}[\rho_{BB}(t)W(\Delta t, \omega_p)]$$

$$= \int d\tau G(t - \tau; \Delta t) \sum_n W[R^* - R_n(t)]. \quad (21)$$

In which the summation is over the members of the trajectory ensemble, and the window is reduced to a spatial function (Gaussian) along the molecular coordinate  $W(R^*)$ , and the finite width of the laser pulse,  $\Delta t$ , is accounted through the Gaussian convolution. The computed signals are shown in Fig. 10. In each case, a swarm of  $n = 31$  trajectories is used, and the probe window of  $0.2 \text{ \AA}$  width is located  $0.1 \text{ \AA}$  to the right of the initial I-I distance:  $R^* = R(t=0) + 0.1 \text{ \AA}$  with  $R(t=0) = 2.72, 2.78$ , and  $2.85 \text{ \AA}$  to simulate excitation at 509, 543, and 585 nm, respectively. The simulations are in good agreement with the experiment. The reproduction of the observed recursions as a function of time and energy establishes that the system is being treated realistically. The extracted vibrational energy relaxation profiles are shown in Fig. 11. At the highest excitation energy, near the dissociation limit of the free molecule,  $2000 \text{ cm}^{-1}$  of energy is lost in the first period of motion; while half as much is lost in a linear fashion during the subsequent 5 ps. In contrast, in the lowest excitation energy, the equivalent of 4 vibrational quanta are transferred to the lattice during  $\sim 15$  periods of

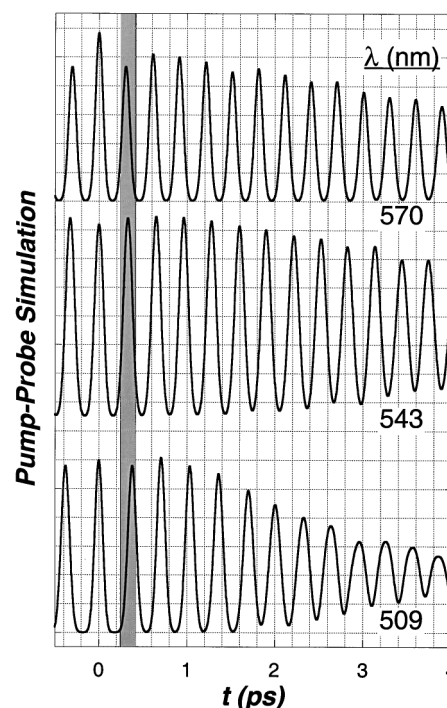


FIG. 10. Simulations of the pump-probe signal using classical dynamics. The results are in good agreement with the experiments (see Fig. 6). The three traces are for ensembles that represent the packets prepared in the strong field SWM and FWM measurements.

motion, without a noticeable change in period. The effective potential in this range is nearly harmonic. These results are in excellent agreement with the experiment, based on a comparison of observed and simulated recursion periods.<sup>50</sup> What is remarkable is that the strong dissipation re-enforces the classical coherence of the system. In the free molecule, excitation at 509 nm would prepare a packet centered at  $v = 50$ , where the level spacing is  $30 \text{ cm}^{-1}$ . Due to the anharmonicity, a broad-band packet at this level would spread in several periods. In contrast, in the solid state, the inelastic collision processes that lead to rapid dissipation also lead to refocusing of the packet.

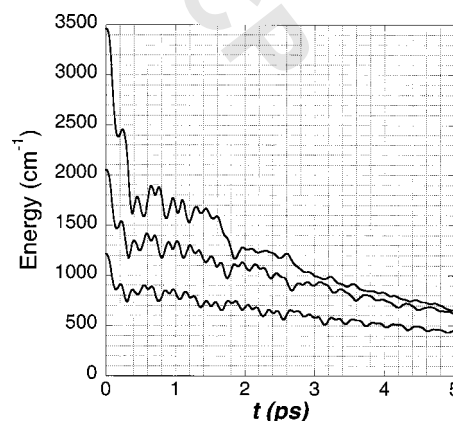


FIG. 11. Vibrational energy loss associated with the swarms used in the simulation of signals in Fig. 10. Top trace:  $\lambda_p = 509 \text{ nm}$ ; middle trace:  $\lambda_p = 543 \text{ nm}$ ; lower trace:  $\lambda_p = 585 \text{ nm}$ .

### D. Vibrational decoherence in the excited state—strong coupling limit

The six-wave signal measures the amplitude level cross correlation between the two vibrational packets prepared on the  $B$ -surface:

$$I(t) = |\langle \varphi_B^{(1)}(-\mathbf{k}_S, t) | \hat{W} | \varphi_B^{(3)}(2\mathbf{k}_P - \mathbf{k}_S, t) \rangle|^2. \quad (22)$$

In the measurement, the first order packet is prepared at  $\lambda_\sigma = 595$  nm, while the third-order packet is created at  $\lambda = 500$  nm ( $2\omega_P - \omega_S$ ), namely at the two extremes of the pump–probe measurements. Based on the timing of the signal, it is clear that the projection window is the same as that of the pump–probe measurements. The SWM signal indicates that the quantum correlation between the two packets survives a full period of motion, despite the transfer of  $\sim 2000$   $\text{cm}^{-1}$  in vibrational energy from chromophore to lattice (system to bath). Evidently, dissipation of the system is not a sufficient criterion for decoherence. In contrast with the impulsive electronic dephasing which occurs in less than a half period, the onset of vibrational decoherence in this case takes time. It occurs during the second period of motion. The sharp recursions in the pump–probe data during this period, and for quite some time to follow, indicate that the diagonal density of the system (chromophore) is maintained. Necessarily, the collapse of the coherence after one period must be ascribed to the decay of the bath coherence. What is being measured is the time for the quantum deterministic motion of chromophore and coupled cage modes to become irreversible. Since the projective measurements are strictly localized on the chromophore (system), information regarding the bath must be encoded in the system-bath entanglement. This is quantified in the explicit simulations that follow.

### E. Semiclassical analysis

In contrast with the ground-state vibrations, rapid dissipation in the excited state implies the absence of a vibrational line spectrum. The strongly coupled environment now selects the coordinate basis as the proper representation, the einstates that can be most naturally described semiclassically. The method we use has been described in detail in an implementation to calculate the closely related three-time correlation in resonant Raman.<sup>13</sup> While well prescribed, the calculation of three-time correlations using forward–backward propagation in full dimensionality is numerically intensive. To reduce the computational overhead, while maintaining the necessary ingredients to dissect the SWM data, we make approximations. The lattice atoms are treated as frozen Gaussians.<sup>51</sup> The molecular coordinate is treated using the Herman–Kluk (HK) propagator<sup>52</sup>

$$\begin{aligned} \hat{U}(t) &= e^{-iHt} \\ &= \int d^N p_0 d^N q_0 J(\mathbf{p}_0, \mathbf{q}_0, t) e^{iS(\mathbf{p}_0, \mathbf{q}_0, t)} |\mathbf{p}_t, \mathbf{q}_t\rangle \langle \mathbf{p}_0, \mathbf{q}_0|. \end{aligned} \quad (23)$$

In which the prefactor,  $J$ , is given by the monodromy matrices that measure the sensitivity of final positions and momenta to their initial values; and  $|\mathbf{p}, \mathbf{q}\rangle$  are coherent states

characterized by their Gaussian width parameter,  $\gamma$ , chosen to be given by the zero-point amplitude on the relaxed  $B$ -state. The explicit propagation is restricted to the interval of vibrational coherence,  $t_{32}$ , with the electronic coherences involved in the preparation and interrogation treated as local projectors that allow shifts in time, position, and momentum along the molecular coordinate. Thus, the three-time correlation of interest is reduced to

$$C(t) = \text{Tr}[\hat{U}(-t) \hat{W}(\Delta t) \hat{U}(t) \rho_{B'B}(t=0)], \quad (24)$$

in which

$$\rho_{B'B}(t=0) = \hat{V}(2\mathbf{k}_P - \mathbf{k}_S) \rho_{XX} \hat{V}^\dagger(-\mathbf{k}_S). \quad (25)$$

With the roles of  $P$ - and  $S$ -pulses reduced to the sudden preparation of  $\rho_{B'B}$  the task is reduced to forward–backward propagation over the interval  $t = t_{32}$

$$\begin{aligned} C(t) &= \frac{1}{n} \sum_{\mathbf{p}_0, \mathbf{q}_0} J_{f-b}(t) e^{i\Delta S_{f-b}(t)/\hbar} \langle \mathbf{p}_0, \mathbf{q}_0 + \mathbf{d}\mathbf{q} | U_{cl} \\ &\quad \times (-t) \hat{W} U_{cl}(t) | \mathbf{p}_0, \mathbf{q}_0 + \mathbf{d}\mathbf{q}' \rangle. \end{aligned} \quad (26)$$

The initial positions and momenta,  $\mathbf{p}_0$  and  $\mathbf{q}_0$  are sampled from a thermal ground-state distribution. The role of the preparation,  $\hat{V}$ , is reduced to vertical projection in momentum,  $\delta[\mathbf{p}_X - \mathbf{p}_B]$ , while the molecular coordinate is shifted to satisfy the Franck–Condon condition,  $\delta[2\omega_P - \omega_S - \Delta V_{BX}(\mathbf{q})]$  for  $\mathbf{q}_0$ , and  $\delta[\omega_P - \Delta V_{BX}(\mathbf{q})]$  for  $\mathbf{q}'_0$ . In (26) the propagator is decomposed into the classical term,  $U_{cl}(t)$ , which evolves momenta and positions; and  $\Delta S_{f-b}(t)$  and  $J_{f-b}(t)$ , which are the classical action and HK prefactor that accumulate around the circuit. Implementation of the window projector, instead of explicit simulation over the excited states involved in the probe transition, requires some thought. What is required is to forward propagate the initial ket up to time  $t$ , to then make a jump in  $\mathbf{p}, \mathbf{q}, \Delta t$ , consistent with the experimental interrogation window, then propagate this projected ket backward in time and correlate it with the initial bra distribution. Such an execution in  $N$ -dimensions is inefficient since most of the jumps will miss the target state after back-propagation. Instead, we first forward propagate both bra and ket in all coordinates for a given time  $t$ . We then execute a jump (radial in phase space) along the molecular coordinate: The molecular ket position and momentum is replaced with that of the forward propagated bra. We then propagate the ket backward in time. This is illustrated in the  $p$ - $q$  plot of the chromophore in Fig. 12. The three traces correspond to forward trajectories of bra and ket, and the backward trajectory of the ket after the jump. Switching of the molecular coordinate, but not the bath, recognizes that the interactions with the radiation field are through the local dipole projector. The choice of the radial jump, which corresponds to the minimum phase space distance, is selected to minimize decoherence due to probing—we are interested in the inherent observable coherence, which can always be spoiled through a bad measurement. The magnitudes of the  $p, q$ , and  $t$  shifts involved in the jump are well within the experimental parameters. To transmit this information, in Fig. 12 we have shaded the track covered by a trajectory under the laser pulse. The time shift in the jump is the

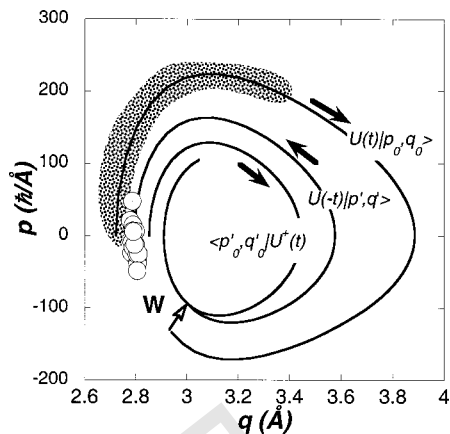


FIG. 12. The molecular trajectory associated with the forward-backward propagation scheme. The ket and bra prepared at 509 and 585 nm are forward propagated. The latter advances in phase angle due to the anharmonicity of the chromophore. The interrogation through the action of the  $P'$  pulse is reduced to the  $W$  projector, which executes a radial jump. Back propagation after the jump leads to the coherent states indicated by the circles. The shaded area of the ket indicates the trail traveled under the laser pulse.

equivalent of the phase angle slip between the forward bra and ket trajectories due to anharmonicity. It can be seen in Fig. 12 that this slip is smaller than the angle swept by the shaded track. It should be obvious from the figure that the same considerations apply for the  $p, q$  shift. The procedure has the desired attributes of forward-backward propagation: All thermally occupied environment modes that are not coupled to the chromophore are perfectly reversed. All coupled modes that evolve harmonically are perfectly reversed. Only coupled modes that evolve anharmonically slip in position and momentum, and accumulate action upon closing the circuit.

That the decay of the SWM signal after one recursion is not due to the trivial loss of phase space overlap in the system coordinate, between the  $S$ - and  $P$ -packets, is evident from the pump-probe data. The classical cross-correlation between two such packets corresponds to the coincidence of signals obtained in two different measurements. This is what is represented by the shaded stripe in Fig. 9, and reproduced in the classical simulations of Fig. 11. In Fig. 12, the coherent states of the swarm are shown as circles after forward-backward propagation for one period. Their phase angle dispersion, i.e., dephasing of the system coordinate, is well within the angle spanned under the probe pulse width—the widths of the observed recursions are dominated by the laser pulse duration. As such, the classical projection contained in the angle bracket in (26) remains near unity. This leaves the irreversible phases,  $\Delta S_{f-b}$ , which accumulate through the many-body action and the HK prefactor  $J_{f-b}$  as the sources for the decay of the correlation (26). A rapid growth in  $J$  would signify the onset of classical chaos. The simulations show that  $J_{f-b}$  grows by a factor of  $\sim 2$  in the first period of motion; but it returns to near unity by the second period, after the molecule reaches the harmonic part of the potential. On the time scale of relevance, the role of the prefactor (which arises as a second order correction to the stationary phase approximation) is secondary. The rapid decay of the

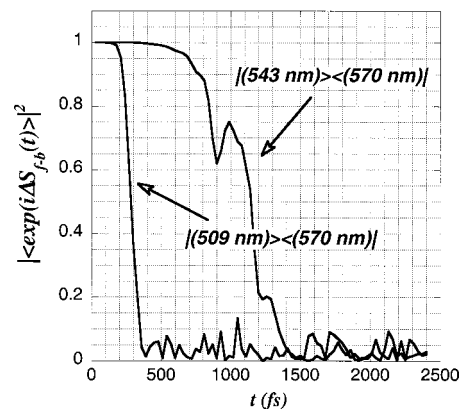


FIG. 13. The simulated decay of the vibrational quantum coherence, as measured through the cross-correlation between ket/bra pairs indicated by the preparation wavelengths. The correlation is constructed from the phase factors due to the accumulated many-body action in the forward-backward propagation, Eq. (27) of text.

correlation (26) can be exclusively associated with the scrambling of the quantum phase, which in the present appears as the accumulation of the many-body action around the closed circuit:

$$C(t) = \frac{1}{n} \sum_{p_0, q_0} e^{i\Delta S_{f-b}(t)/\hbar}. \quad (27)$$

In Fig. 13 we provide plots of the correlation (27) between ket/bra pairs identified by their preparation wavelengths,  $|509\rangle\langle 585|$  and  $|543\rangle\langle 585|$ . These are the quantum cross-correlations between packets for which individually energy loss profiles were given in Fig. 11. The first of these cross-correlation corresponds to the coherence observable in SWM, while the second would correspond to the coherence observable through the  $P^{(1,2)}$  contribution in FWM, in the same experiment. In the first case, the quantum coherence decays in 400 fs, in excellent agreement with the experiment. In the second case, the coherence survives for 4 periods (1200 fs). Although this signal is difficult to establish experimentally, due to the strong interference observed in the strong-field FWM signal (see Fig. 9), it provides a useful reference for mechanistic analysis. The spread of the forward-backward phase,  $\Delta\Omega_{f-b} = \Delta S_{f-b}(\text{mod } \pi)$ , associated with the two different preparations is shown in Fig. 14. In this representation, decoherence is marked by the  $2\pi$ -spread of the accumulated angle. Note, the forward-backward propagation is carried out for the universe (chromophore+environment), and as such the time propagation is unitary, and the classical action is reversible. Irreversibility sets in because the projector sandwiched between the forward and backward propagator in (24) is local, it acts on the chromophore but not the bath. Had we carried out a jump in all coordinates, the time reversed ket in Fig. 12 would have regained all of its energy to terminate at the initial conditions of the forward-bra. With this in mind, we comment on the features observed in Fig. 14.

- (a) In the first 200 fs, the evolution is coherent, despite the fact that significant energy is lost to the lattice (see Fig. 11). This initial motion is completely reversible in the



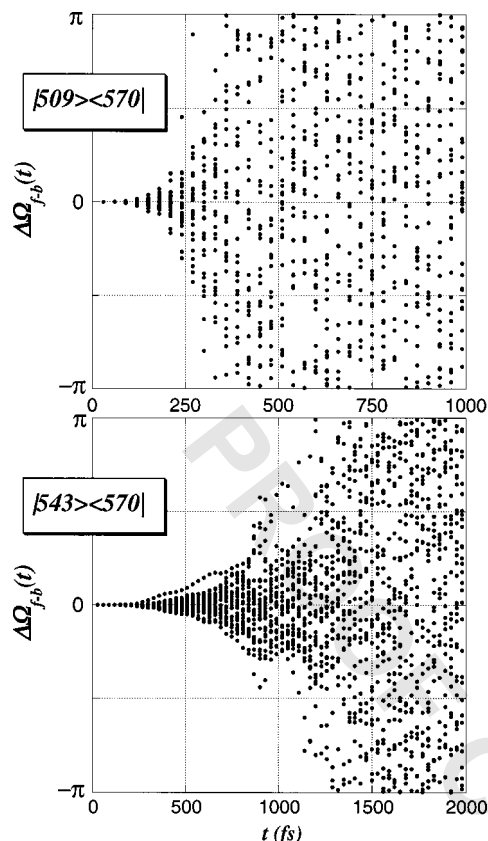


FIG. 14. The dispersion in phase angle due to accumulated many-body action. The correlations are for the set of trajectories for which the energy loss as a function of time is given in Fig. 11.

forward–backward sense. The bath modes that have accepted the energy are evolving deterministically—they are doing work.

- (b) In the high-energy collision, the phase angle spread is triggered by the collision at  $t \sim 250$  fs, and decoherence is complete by the time the molecule rebounds at  $t = 400$  fs. While the same events are discernible in the low-energy collision, the magnitude of the spread in angle is significantly smaller, and decoherence is delayed to  $t = 1.5$  ps. The quantitative difference between the two events is the extent of the anharmonicity of the immediately driven modes. In the high-energy collision, the solvated chromophore potential develops a shelflike outer branch (see Fig. 1) due to the near cancellation between the intramolecular attraction and intermolecular repulsion. As the molecule stretches, it drives the cage modes to sufficiently large amplitude to sample the anharmonic part of their interactions. The strong anharmonicity of chromophore and driven cage modes leads to the large dispersion of the accumulated quantum phase by the different members of the ensemble. In the lower energy collision, both chromophore and cage modes are more harmonic, as such, the collective dynamics retains quantum coherence over several periods.
- (c) In the low-energy collision, the decoherence is triggered shortly after 1 ps. This is the time associated with the recoil of the primary cage atoms. As the first shell

rebounds from its collision with the second shell, the information lost to the secondary bath modes is communicated to the chromophore. The irreversibility is now set in by the multiplicity of coupled modes, and therefore through the dispersion of histories of evolution in the environment.<sup>26</sup>

## VI. CONCLUSIONS

We have presented a set of measurements that allow the dissection of vibrational decoherence in the model system of  $I_2$  isolated in solid Ar. Many of the important conclusions can be drawn with operative definitions that are based on experiments alone. On the ground electronic state, TRCARS measurements show that the vibrational coherence decays after hundreds of periods of motion (10 ps near  $v = 7$ ), establishing that the weak coupling limit, in which decoherence is rate limited by the dephasing of the system. Electronic dephasing between the X- and B-states occurs on the time scale of 100 fs (based on intensities of overtones in the resonant Raman progression), on a time scale shorter than any intramolecular or intermolecular vibrational period. The presented six-wave measurements overcome the electronic dephasing time window, and allow probing of vibrational coherences on the excited B-state. This is accomplished through a parametric six-wave mixing scheme that yields the amplitude level cross-correlation between a pair of packets launched on the B-state. For the particular pair of packets selected, the coherence survives for one recursion, during which the  $\sim 2000 \text{ cm}^{-1}$  of energy is lost of the cage. The rate of energy loss is established through pump–probe measurements through the same resonances, which show that the classical vibrational coherence lasts long after collapse of the quantum coherence. Classical simulations are used to reproduce the pump–probe data, while semiclassical simulations are used to analyze quantum decoherence in the strong coupling limit.

The various observables, and the role of measurement on observables, are defined through time circuit-diagrams, which highlight quantum coherence as a measure of the reversibility of quantum dynamics around a closed circuit. The diagrams also provide the recipe for the computation of observables through semiclassical simulations and underscore the rationale for forward–backward implementation. Decoherence occurs because the measurements (preparation and interrogation) are carried out through local projectors that act on the system coordinates, while time reversal invariance is reserved for the unitary evolution of system+bath. The simulations, using the HK propagator for the system and frozen Gaussians for the bath, are in excellent agreement with the experiments. In this strong coupling limit, on the time scale of relevance, the decay can be exclusively ascribed to the dispersion of the many-body classical action accumulated after forward–backward evolution. The dispersion arises from the driven anharmonic bath coordinates, while the strong dissipation re-enforces classical coherence on the system. Although the measurements are local to the system, information about the bath is passed on through the quantum phase dictated by the many-body action, which describes the entanglement of the system with the bath.



The measurements also have implications with regard to control. Using chirped pulses, it has previously been demonstrated that when prepared in the harmonic region of the excited-state potential, the classical dynamics is controllable.<sup>53</sup> In this regard, the action of chirped pulses can be understood as the launching of an energy-ordered set of classical trajectories.<sup>54</sup> As long as the dissipation is linear, the chirp rate can be adjusted to compensate for anharmonicity, to effect wavepacket focusing or defocusing. The present results indicate that with the use of shaped pulses, interferometric quantum control of the excited state vibrations can be implemented, as long as this is carried out within the coherence window in time.

## ACKNOWLEDGMENTS

This research was funded through a grant from the U.S. AFOSR (F49620-01-1-0449). Valuable discussions with J. A. Cina during the proofing of the manuscript are gratefully acknowledged.

<sup>1</sup>For a recent review, see J. C. Wright, *Int. Rev. Phys. Chem.* **21**, 185 (2002).

<sup>2</sup>For an analysis of interferometric multilinear spectroscopies, see: J. A. Cina, D. S. Kilin, and T. S. Humble, *J. Chem. Phys.* (to be published).

<sup>3</sup>W. H. Zurek, *Phys. Today* **44**, 36 (1991).

<sup>4</sup>D. Giuliani, E. Joos, C. Keifer, J. Kupsch, I. O. Stamatescu, and H. D. Zeh, *Decoherence and the Appearance of a Classical World in Quantum Theory* (Springer Verlag, Berlin, 1996).

<sup>5</sup>J. R. Anglin, J. P. Paz, and W. H. Zurek, **55**, 4041 (1997).

<sup>6</sup>A. J. Leggett, *J. Phys.: Condens. Matter* **14**, R415 (2002).

<sup>7</sup>S. A. Rice and M. Zhao, *Optical Control of Molecular Dynamics* (Wiley Interscience, New York, 2000); D. J. Tannor and S. A. Rice, *J. Chem. Phys.* **83**, 5013 (1985).

<sup>8</sup>M. A. Nielsen and I. L. Chuang, *Quantum Computation and Quantum Information* (Cambridge University Press, Cambridge, 2000).

<sup>9</sup>Parametric refers to processes in which the photon energy and the material energy are separately conserved, and as such are described by a real susceptibility. See, for example, R. W. Boyd, *Nonlinear Optics* (Academic, New York 1992), p. 14.

<sup>10</sup>W. H. Miller, *J. Phys. Chem. A* **105**, 2942 (2001), and references therein.

<sup>11</sup>M. Ovchinnikov and V. A. Apkarian, *J. Chem. Phys.* **105**, 10312 (1996); **108**, 2277 (1998).

<sup>12</sup>O. Kuhn, N. Makri, *J. Phys. Chem. A* **103**, 9487 (1999).

<sup>13</sup>M. Ovchinnikov and V. A. Apkarian, *J. Chem. Phys.* **106**, 5775 (1997).

<sup>14</sup>M. Ovchinnikov, V. A. Apkarian, and G. A. Voth, *J. Chem. Phys.* **114**, 7130 (2001).

<sup>15</sup>J. Almy, K. Kizer, R. Zadoyan, and V. A. Apkarian, *J. Phys. Chem. A* **104**, 3508 (2000).

<sup>16</sup>M. Karavitis, R. Zadoyan, and V. A. Apkarian, *J. Chem. Phys.* **114**, 4131 (2001).

<sup>17</sup>M. Karavitis, D. Segale, Z. Bihary, M. Pettersson, and V. A. Apkarian, *Low Temp. Phys.* **29**, 1071 (2003).

<sup>18</sup>W. F. Howard and L. J. Andrews, *J. Raman Spectrosc.* **2**, 442 (1974); J. Grzybowski and L. J. Andrews, *ibid.* **4**, 99 (1975); L. Andrews, *Appl. Spectrosc.* **11**, 125 (1976).

<sup>19</sup>A. J. Leggett, S. Chakravarty, A. T. Dorsey, M. P. A. Fisher, A. Garg, and W. Zwerger, *Rev. Mod. Phys.* **59**, 1 (1987).

<sup>20</sup>R. Zadoyan, M. Sterling, and V. A. Apkarian, *J. Chem. Soc., Faraday Trans.* **92**, 1821 (1996).

<sup>21</sup>R. Zadoyan, J. Almy, and V. A. Apkarian, *J. Chem. Soc. Far. Disc.* **108**, 255 (1997).

<sup>22</sup>J. A. Wheeler and W. H. Zurek, *Quantum Theory and Measurement* (Princeton University Press, Princeton, NJ, 1983).

<sup>23</sup>E. Schmidt, *Math. Ann.* **63**, 433 (1907).

<sup>24</sup>A. Albrecht, *Phys. Rev. D* **46**, 5504 (1992).

<sup>25</sup>H. D. Zeh, *Found. Phys.* **1**, 69 (1970); **3**, 109 (1973).

<sup>26</sup>J. P. Paz, S. Habib, and W. H. Zurek, *Phys. Rev. D* **47**, 488 (1993).

<sup>27</sup>G. A. Fiete and E. J. Heller, *Phys. Rev. A* **68**, 022112 (2003).

<sup>28</sup>Y. Tanimura and S. Mukamel, *J. Chem. Phys.* **99**, 9496 (1993).

<sup>29</sup>D. J. Ulness, J. C. Kirkwood, and A. C. Albrecht, *J. Chem. Phys.* **108**, 3897 (1998); J. C. Kirkwood and A. C. Albrecht, *Phys. Rev. A* **61**, 043803 (2000); *J. Raman Spectrosc.* **31**, 107 (2000).

<sup>30</sup>L. J. Kaufman, J. Y. Heo, L. D. Ziegler, and G. R. Fleming, *Phys. Rev. Lett.* **88**, 207402 (2002).

<sup>31</sup>O. Golonzka, N. Demirdoven, M. Khalil, and A. Tokmakoff, *J. Chem. Phys.* **113**, 9893 (2000).

<sup>32</sup>K. J. Kubarych, C. J. Milne, S. Lin, V. Astinov, and R. J. D. Miller, *J. Chem. Phys.* **116**, 2016 (2002).

<sup>33</sup>S. Mukamel, *Principles of Optical Nonlinear Spectroscopy* (Oxford University Press, New York, 1999).

<sup>34</sup>W. Domcke and G. Stock, *Adv. Chem. Phys.* **100**, 1 (1997).

<sup>35</sup>D. J. Tannor, S. A. Rice, and P. M. Weber, *J. Chem. Phys.* **83**, 6158 (1985).

<sup>36</sup>For a comparative discussion of the various diagrams in FWM, see: B. I. Grimberg, V. Lozovoy, M. Dantus, and S. Mukamel, *J. Phys. Chem. A* **106**, 697 (2002).

<sup>37</sup>M. Thoss, H. B. Wang, and W. H. Miller, *J. Chem. Phys.* **114**, 9220 (2001); H. B. Wang, M. Thoss, K. L. Sogge, R. Gelabert, X. Gimenez, and W. H. Miller, *ibid.* **114**, 2562 (2001).

<sup>38</sup>E. Jezek, N. Makri, *J. Phys. Chem. A* **105**, 2851 (2001); J. Shao and N. Makri, *J. Chem. Phys.* **113**, 3681 (2000).

<sup>39</sup>R. Zadoyan, D. Kohen, D. Lidar, and V. A. Apkarian, *Chem. Phys.* **266**, 323 (2001).

<sup>40</sup>R. Zadoyan and V. A. Apkarian, *Chem. Phys. Lett.* **326**, 1 (2000).

<sup>41</sup>J. Faeder, I. Pinkas, G. Knopp, Y. Prior, and D. J. Tannor, *J. Chem. Phys.* **115**, 8440 (2001).

<sup>42</sup>L. E. Fried and S. Mukamel, *J. Chem. Phys.* **93**, 3063 (1990).

<sup>43</sup>R. Zadoyan, Z. Li, C. Martens, P. Ashjian, and V. A. Apkarian, *Chem. Phys. Lett.* **218**, 504 (1994).

<sup>44</sup>Z. M. Li, J. Y. Fang, and C. C. Martens, *J. Chem. Phys.* **104**, 6919 (1996).

<sup>45</sup>Y. C. Shen and J. A. Cina, *J. Chem. Phys.* **110**, 9793 (1999).

<sup>46</sup>A. V. Benderskii, R. Zadoyan, and V. A. Apkarian, *J. Chem. Phys.* **107**, 8437 (1997).

<sup>47</sup>M. Macler and M. C. Heaven, *Chem. Phys.* **151**, 219 (1991).

<sup>48</sup>W. H. Zurek, *Phys. Rev. D* **24**, 1516 (1981).

<sup>49</sup>M. Bargheer, M. Gühr, P. Dietrich, and N. Schwentner, *Phys. Chem. Chem. Phys.* **4**, 75 (2002).

<sup>50</sup>Z. Bihary, M. Karavitis, R. Zadoyan, and V. A. Apkarian, *J. Chem. Phys.* (to be published).

<sup>51</sup>E. J. Heller, *J. Chem. Phys.* **94**, 2723 (1991).

<sup>52</sup>M. F. Herman and E. Kluk, *Chem. Phys.* **91**, 27 (1984); E. Kluk, M. F. Herman, and H. L. Davis, *J. Chem. Phys.* **84**, 326 (1986); M. F. Herman, *ibid.* **85**, 2069 (1986).

<sup>53</sup>J. W. Che, M. Messina, K. R. Wilson, V. A. Apkarian, Z. Li, C. C. Martens, R. Zadoyan, and Y. J. Yan, *J. Phys. Chem.* **100**, 7873 (1996); C. J. Bardeen, J. W. Che, K. R. Wilson, V. Yakovlev, V. A. Apkarian, C. C. Martens, R. Zadoyan, B. Kohler, and M. Messina, *J. Chem. Phys.* **106**, 8486 (1997).

<sup>54</sup>M. Sterling, R. Zadoyan, and V. A. Apkarian, *J. Chem. Phys.* **104**, 6497 (1996).